Size and temperature effects on electric properties of CdTe/ZnTe quantum rings*

Woo-Pyo Hong† and Seoung-Hwan Park

Department of Electronics Engineering, Catholic University of Daegu, Hayang, Kyeongbuk 712-702, Korea

(Received 30 March 2011; revised manuscript received 13 April 2011)

The electronic properties of CdTe/ZnTe quantum rings (QRs) are investigated as functions of size and temperature using an eight-band strain-dependent $\boldsymbol{k}\cdot\boldsymbol{p}$ Hamiltonian. The size effects of diameter and height on the strain distributions around the QRs are studied. We find that the interband transition energy, defined as the energy difference between the ground electronic and the ground heavy-hole subbands, increases with the increasing QR inner diameter regardless of the temperature, while the interband energy decreases with the increasing QR height. This is attributed to the reduction of subband energies in both the conduction and the valence bands due to the strain effects. Our model, in the framework of the finite element method and the theory of elasticity of solids, shows a good agreement with the temperature-dependent photoluminescence measurement of the interband transition energies.

Keywords: quantum ring, eight-band $\boldsymbol{k}\cdot\boldsymbol{p}$ model, finite-element method, strain and temperature effects, electronic structure

PACS: 85.60.Bt, 85.30.De, 85.30.Tv, 78.20.Bh **DOI:** 10.1088/1674-1056/20/9/098502

1. Introduction

Among nanoscale semiconductor heterostructures of varying shapes and sizes, quantum dots (QDs) and quantum rings (QRs) have been attractive low-dimensional semiconductor structures for both the fundamental physical property study and the potential applications in optoelectronic devices. QRs have recently received much attention due to unique physical properties, such as the Aharonov–Bohm effect,[1] the existence of a negative excitonic permanent dipole moment,[2] and their practical applications in quantum information processing[3] and terahertz devices.[4]

As candidate substances for nanoscale semiconductor heterostructure fabrication, the II–VI materials have recently attracted increasing attention due to their large band gaps and their potential applications in short-wavelength optoelectronic devices. Among them, the CdTe/ZnTe material system is interesting for the fabrication of QDs and QRs, because the lattice mismatch between these two constituents is similar to that in the InAs/GaAs system, which is the most widely studied system in the context of QDs.[5−7] In addition, wide-bandgap CdTe QDs and QRs with higher excitonic binding energies are extremely advantageous for potential applications in optoelectronics devices operating in the green region of the spectrum.[8,9] Advances in the growth technology of II–VI semiconductors now permit the growth of high-quality CdTe/ZnTe QDs[8−13] and QRs.[14]

On the theoretical side, understanding how the structural elements of the semiconductor heterostructure, such as the capping and the wetting layers, affect the strain distribution and subsequently the electronic and optical properties is an interesting issue. We recently analysed the electronic and optical properties of QDs based on the linear elasticity theory of solids and the eight-band $\boldsymbol{k}\cdot\boldsymbol{p}$ Hamiltonian,[15,16] and studied how the three-dimensional strain fields induced around the CdTe/ZnTe QDs affect the conduction and the valence subband energies.[15,16] It was demonstrated that for a fixed capping layer thickness, the transition energy between the ground states in the conduction and the valance subbands decreased with the increasing wetting layer thickness. On the other hand, the transition energy shifted upward as the capping layer thickness was increased, regardless of the thickness of the wetting layer.[15,16] The QD structure and the mole fraction of the QD were shown to strongly affect the optical gain of the CdTe/ZnTe QD.[17−20] We expect similar structural effects to occur in the electric and the optical properties of the

*Project supported by the Basic Science Research Program through the National Research Foundation of Korea (NRF) and the Ministry of Education, Science, and Technology, Korea (Grant No. 2010-0024703).

†Corresponding author. E-mail: wphong@cu.ac.kr

© 2011 Chinese Physical Society and IOP Publishing Ltd

CdTe/ZnTe QRs.

In this paper, based on our numerical model for QD systems,[15−20] we study the size effects of the structural parameters including the diameter and the height of CdTe/ZnTe QRs on the strain distributions. Then, we investigate how the structural parameters and the temperature of the system affect the interband transition energy of the QR, which is defined as the energy difference between the ground electronic subband and the ground heavy-hole subband,[14] while fixing other system constituents including the wetting and the capping layers. We show that the transition energy increases with decreasing QR size, regardless of the temperature of the QR. Furthermore, we demonstrate that the interband transition energy decreases with increasing QR temperature, which is in good accordance with those obtained from the temperature-dependent photoluminescence (PL) measurement.[14]

2. Theory

The energy levels and the wave functions of bounded electron and hole states are calculated with the eight-band $\boldsymbol{k}\cdot\boldsymbol{p}$ model. The effective-mass Hamiltonian H_0 is given by[21]

$$H_0=\begin{pmatrix} A & 0 & -\sqrt{3}V^\dagger & \sqrt{2}U & V & 0 & U & \sqrt{2}V \\ 0 & A & 0 & -V^\dagger & \sqrt{2}U & \sqrt{3}V & \sqrt{2}V^\dagger & -U \\ -\sqrt{3}V & 0 & -(P+Q) & S & -R & 0 & \frac{1}{\sqrt{2}}S & -\sqrt{2}R \\ \sqrt{2}U^\dagger & -V & S^\dagger & -(P-Q) & 0 & -R & \sqrt{2}Q & -\sqrt{3/2}S \\ V^\dagger & \sqrt{2}U^\dagger & -R^\dagger & 0 & -(P-Q) & -S & -\sqrt{3/2}S^\dagger & -\sqrt{2}Q \\ 0 & \sqrt{3}V^\dagger & 0 & -R^\dagger & -S^\dagger & -(P+Q) & \sqrt{2}R^\dagger & \frac{1}{\sqrt{2}}S^\dagger \\ U^\dagger & \sqrt{2}V & \frac{1}{\sqrt{2}}S^\dagger & \sqrt{2}Q & -\sqrt{3/2}S & \sqrt{2}R & -(P+\Delta) & 0 \\ \sqrt{2}V^\dagger & -U^\dagger & -\sqrt{2}R^\dagger & -\sqrt{3/2}S^\dagger & -\sqrt{2}Q & \frac{1}{\sqrt{2}}S & 0 & -(P+\Delta) \end{pmatrix}\begin{matrix} |1\rangle \\ |2\rangle \\ |3\rangle \\ |4\rangle \\ |5\rangle \\ |6\rangle \\ |7\rangle \\ |8\rangle \end{matrix}, \tag{1}$$

where

$$\begin{aligned} A &= E_{\rm g}-\frac{\hbar^2}{2m_{\rm c}}\left(\frac{\partial^2}{\partial x^2}+\frac{\partial^2}{\partial y^2}+\frac{\partial^2}{\partial z^2}\right)+V_{\rm e},\\ V &= \frac{P_0}{\sqrt{6}}\left(\frac{\partial}{\partial x}-{\rm i}\frac{\partial}{\partial y}\right),\\ U &= \frac{P_0}{\sqrt{3}}\frac{\partial}{\partial z},\\ P &= -\frac{\hbar^2\gamma_1}{2m_0}\left(\frac{\partial^2}{\partial x^2}+\frac{\partial^2}{\partial y^2}+\frac{\partial^2}{\partial z^2}\right)+V_{\rm h},\\ Q &= -\frac{\hbar^2\gamma_2}{2m_0}\left(\frac{\partial^2}{\partial x^2}+\frac{\partial^2}{\partial y^2}-2\frac{\partial^2}{\partial z^2}\right),\\ S &= -\frac{\hbar^2\gamma_3}{2m_0}2\sqrt{3}\left(\frac{\partial}{\partial x}-{\rm i}\frac{\partial}{\partial y}\right)\frac{\partial}{\partial z},\\ R &= \frac{\hbar^2}{2m_0}\sqrt{3}\left[\gamma_2\left(\frac{\partial^2}{\partial x^2}-\frac{\partial^2}{\partial y^2}\right)-2{\rm i}\gamma_3\frac{\partial}{\partial x}\frac{\partial}{\partial y}\right]. \end{aligned} \tag{2}$$

The basis set is summarized as follows

$$\begin{aligned} |1\rangle &= |c1\rangle : |S\rangle\uparrow,\\ |2\rangle &= |c2\rangle : |S\rangle\downarrow,\\ |3\rangle &= |h1\rangle : \left|\frac{3}{2},\frac{3}{2}\right\rangle = -\frac{1}{\sqrt{2}}[|X\rangle+{\rm i}|Y\rangle]\uparrow,\\ |4\rangle &= |l1\rangle : \left|\frac{3}{2},\frac{1}{2}\right\rangle = -\frac{1}{\sqrt{6}}[(|X\rangle+{\rm i}|Y\rangle)\downarrow-2|Z\rangle\uparrow],\\ |5\rangle &= |l2\rangle : \left|\frac{3}{2},-\frac{1}{2}\right\rangle = \frac{1}{\sqrt{6}}[(|X\rangle-{\rm i}|Y\rangle)\uparrow+2|Z\rangle\downarrow],\\ |6\rangle &= |h2\rangle : \left|\frac{3}{2},-\frac{3}{2}\right\rangle = \frac{1}{\sqrt{2}}[|X\rangle-{\rm i}|Y\rangle]\downarrow,\\ |7\rangle &= |s1\rangle : \left|\frac{1}{2},\frac{1}{2}\right\rangle = \frac{1}{\sqrt{3}}[(|X\rangle+{\rm i}|Y\rangle)\downarrow+|Z\rangle\uparrow],\\ |8\rangle &= |s2\rangle : \left|\frac{1}{2},-\frac{1}{2}\right\rangle\\ &= \frac{1}{\sqrt{3}}[(|X\rangle-{\rm i}|Y\rangle)\uparrow-|Z\rangle\downarrow]. \end{aligned} \tag{3}$$

Here, P_0 is the coupling between the conduction and the valence bands, γ_1, γ_2, and γ_3 are the Luttinger parameters, and Δ is the spin-orbit split-off energy. The band gap energy is given by $E_{\rm g}=E_{\rm c}-E_{\rm v}$, where $E_{\rm c}$ and $E_{\rm v}$ are the unstrained conduction- and valence-band energies, respectively. The electron potential $V_{\rm e}(x,y,z)$ and the hole potential $V_{\rm h}(x,y,z)$ are respectively defined as

$$V_{\rm e}(x,y,z)=\begin{cases}0, & \text{inside ring},\\ V_{\rm e0}, & \text{otherwise},\end{cases} \tag{4}$$

and

$$V_{\rm h}(x,y,z)=\begin{cases}0, & \text{inside ring},\\ V_{\rm h0}, & \text{otherwise}.\end{cases} \tag{5}$$

The strain part of the Hamiltonian is given by

$$H_\epsilon = \begin{pmatrix} A_\epsilon & 0 & \sqrt{3}v^* & -\sqrt{2}u & -v & 0 & -u & -\sqrt{2}v \\ 0 & A_\epsilon & 0 & v^* & -\sqrt{2}u & -\sqrt{3}v & \sqrt{2}v^* & u \\ \sqrt{3}v & 0 & -(P_\epsilon + Q_\epsilon) & S_\epsilon & -R_\epsilon & 0 & \frac{1}{\sqrt{2}}S_\epsilon & -\sqrt{2}R_\epsilon \\ -\sqrt{2}u^* & v & S_\epsilon^* & -(P_\epsilon - Q_\epsilon) & 0 & -R_\epsilon & \sqrt{2}Q_\epsilon & -\sqrt{3/2}S_\epsilon \\ -v^* & -\sqrt{2}u^* & -R_\epsilon^* & 0 & -(P_\epsilon - Q_\epsilon) & -S_\epsilon & -\sqrt{3/2}S_\epsilon^* & -\sqrt{2}Q_\epsilon \\ 0 & -\sqrt{3}v^* & 0 & -R_\epsilon^* & -S_\epsilon^* & -(P_\epsilon + Q_\epsilon) & \sqrt{2}R_\epsilon^* & \frac{1}{\sqrt{2}}S_\epsilon^* \\ -u^* & -\sqrt{2}v & \frac{1}{\sqrt{2}}S_\epsilon^* & \sqrt{2}Q_\epsilon & -\sqrt{3/2}S_\epsilon & \sqrt{2}R_\epsilon & -(P_\epsilon + \Delta) & 0 \\ -\sqrt{2}v^* & u^* & -\sqrt{2}R_\epsilon^* & -\sqrt{3/2}S_\epsilon^* & -\sqrt{2}Q_\epsilon & \frac{1}{\sqrt{2}}S_\epsilon & 0 & -(P_\epsilon + \Delta) \end{pmatrix}, \quad (6)$$

with

$$\begin{aligned} A_\epsilon &= a_{\rm c}(\epsilon_{xx} + \epsilon_{yy} + \epsilon_{zz}), \\ v &= \frac{P_0}{\sqrt{6}} \sum_j (\epsilon_{xj} - {\rm i}\epsilon_{yj}) \frac{\partial}{\partial x_j}, \\ u &= \frac{P_0}{\sqrt{3}} \sum_j \epsilon_{zj} \frac{\partial}{\partial x_j}, \\ P_\epsilon &= -a_{\rm v}(\epsilon_{xx} + \epsilon_{yy} + \epsilon_{zz}), \\ Q_\epsilon &= -\frac{b}{2}(\epsilon_{xx} + \epsilon_{yy} - 2\epsilon_{zz}), \\ S_\epsilon &= -d(\epsilon_{xz} - {\rm i}\epsilon_{yz}), \\ R_\epsilon &= \frac{\sqrt{3}}{2} b(\epsilon_{xx} - \epsilon_{yy}) - {\rm i}d\epsilon_{xy}. \end{aligned} \quad (7)$$

where ϵ_{ij} is the symmetric strain tensor, b and d are the shear deformation potentials, $a_{\rm v}$ is the hydrostatic valence-band deformation potential, and $a_{\rm c}$ is the conduction-band deformation potential. All relevant parameters for the model are summarized in Table 1.

Table 1. Physical parameters used in the calculation.

Parameters	ZnTe	CdTe
Lattice constant[22]		
a/Å	6.08	6.48
Energy parameter		
$E_{\rm g}$[23]/eV	2.7	1.496
Δ[24]/eV	0.93	0.91
Valence band effective-mass parameters[25]		
γ_1	4.789	4.67
γ_2	1.201	1.314
γ_3	1.873	1.880
Deformation potentials[24]		
$a_{\rm c}$/eV	–5.83	–3.96
$a_{\rm v}$/eV	0.79	0.55
b/eV	–1.26	–1.1
d/eV	–4.6	–4.8
Conduction bandoffset ratio[23]		
	0.75	
Elastic modulus[26,27]		
C_{11}/GPa	72.2	53.8
C_{12}/GPa	40.9	37.4
C_{44}/GPa	30.8	20.1

According to the theory of linear elasticity, the stress–strain relationship (the constitutive equation) for linear conditions including initial stress and strain is given as

$$\sigma_{ij} = \mathcal{C}_{ijkl}(\epsilon_{kl} - (\epsilon_0)_{kl}), \quad i,j,k,l = x,y,z, \quad (8)$$

where $\mathcal{C}_{ijkl}$ is the component of the fourth-order elastic moduli tensor.[28] We adopt the finite element method (FEM) procedures[29–31] to find how the strain fields under the boundary values due to the initial mismatch strains between the ZnTe substrate and the CdTe wetting layer and between the CdTe QR and the ZnTe capping layer distribute through out the whole QR system. The initial mismatch strains are taken as

$$(\epsilon_0)_{xx} = (\epsilon_0)_{yy} = \frac{a_{\rm s} - a_{\rm d}}{a_{\rm d}}, \quad \epsilon_{zz} = -\frac{2C_{12}}{C_{11}}(\epsilon_0)_{xx}, \quad (9)$$

where $a_{\rm s}$ (6.08 Å) and $a_{\rm d}$ (6.48 Å) are the lattice constants of the substrate, the capping layers (ZnTe) and the wetting layer, the QR (CdTe), respectively. Initial mismatch parameters $(\epsilon_0)_{xx}$, $(\epsilon_0)_{yy}$, and $(\epsilon_0)_{zz}$ are considered as the initial normal strains in the x, y, and z directions, respectively. The presence of initial $(\epsilon_0)_{zz}$ is due to the Poisson effect: the compressive strains from the lateral directions (ϵ_{xx} and ϵ_{yy}) are so dominant that the strain along the z axis turns out to be tensile.[32]

3. Results and discussion

Figures 1(a) and 1(b) show cross section plots for strain distributions ϵ_{yy} and ϵ_{zz} respectively in the y–z plane of the QR with the following structural parameters. The thickness of the capping layer is $h_{\rm c} = 1000$ Å, the inner and the outer diameters of the QR are $R_1 = 327$ Å and $R_2 = 650$ Å, respectively, and the height of the QR is $h_{\rm r} = 42$ Å. By taking the QR size reported in Ref. [14], the substrate thickness is $h_{\rm s} = 1000$ Å, and the wetting layer thickness

is $h_{\rm w} = 4.5$ ML (1 ML=2.6 Å for CdTe). These parameters are indicated in Fig. 1(a). In the rest of this paper, we set the spatial coordinates in the angstrom unit. We notice from Fig. 1(a) that ϵ_{yy} is compressive inside the QR and tensile around its vicinity denoted by blue and red colours, respectively, and is tensile in the wetting layer. The maximum values of compressive and tensile strains are shown to occur around the interfaces between the CdTe QR and the ZnTe barrier, i.e., at $R = R_1$ and $R = R_2$. For the case of ϵ_{zz} shown in Fig. 1(b), the maximum tensile strain is observed around the top area of the QR ($R = R_1$), meanwhile the completely compressive strain is found in the wetting layer. Figure 1(c), for example, shows ϵ_{xx}, ϵ_{yy}, and ϵ_{zz} distributions at the top of the wetting layer, i.e., at $z = 0$ along the y axis. Inside the QR area, i.e., $R_1 \leq R \leq R_2$, for the case of ϵ_{zz} (dot-dashed line), the strain is compressive, since the compressive strain in the wetting layer influences the QR. On the other hand, for the cases of ϵ_{xx} (dotted line) and ϵ_{yy} (solid line), both strains abruptly change from compressive to tensile once across the QR region.

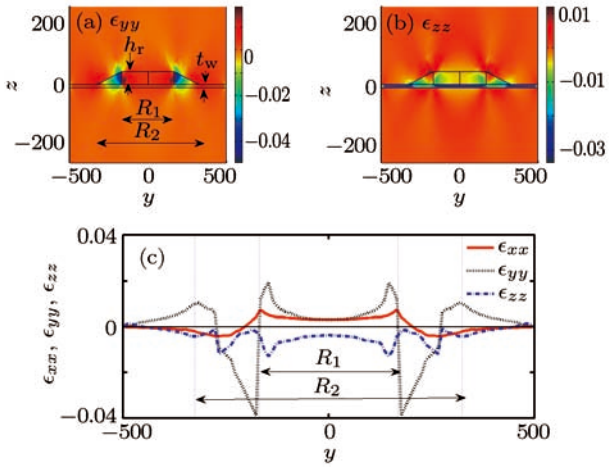


Fig. 1. (colour online) Cross section plots of (a) ϵ_{yy} and (b) ϵ_{zz} in the y–z plane. (c) Plots of strain distributions at $z = 0$ along the y axis. The vertical dotted lines indicate the inner and the outer diameters of the QR. The structural parameters are specified in panel (a).

Figure 2(a) and 2(b) show cross section plots for hydrostatic $\epsilon_{\rm h} = \epsilon_{xx} + \epsilon_{yy} + \epsilon_{zz}$ and bi-axial $\epsilon_{\rm b} = \epsilon_{zz} - (\epsilon_{xx} + \epsilon_{yy})/2$ strains, respectively, which are related to the conduction and the valence subband potentials in Eq. (7). The bi-axial distribution shows the maximum tensile strain at $R = R_1$ near the top of the QR. For the hydrostatic strain case, it is compressive both in the QR and the wetting layer, while it is surrounded by the tensile strain distribution with the maximum tensile strain at $R < R_1$. It is clearly seen in Fig. 2(c) that $\epsilon_{\rm h}$ at $z = 0$ along the y axis is mostly compressive inside the ring and tensile outside of the QR, while ϵ_b changes from compressive to tensile at $R_1 \leq R \leq R_2$. These nontrivial strain distributions strongly affect the conduction and the valence subband energy structures, which can be seen below.

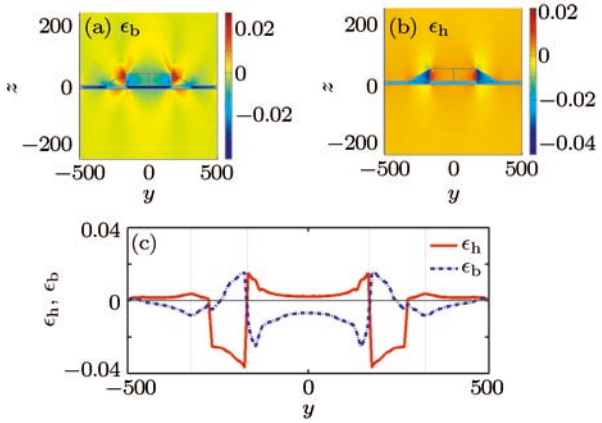


Fig. 2. (colour online) Cross section plots of (a) hydrostatic $\epsilon_{\rm h}$ and (b) bi-axial $\epsilon_{\rm b}$ strains in the y–z plane. (c) Plots of hydrostatic and bi-axial strains at $z = 0$ along the y axis.

We now turn to the size effect of the QR on the strain distributions. It was previously demonstrated for CdTe/ZnTe QD heterostructures[15–20] that the size and the material constituents of the wetting, the capping, and the substrate layers strongly influence the strain distributions and subsequently the energy structures. Figures 3(a) and 3(b) show $\epsilon_{\rm h}$ and ϵ_b at $z = 0$ along the y axis respectively for different QR heights with the same structural parameters as those in Fig. 1.

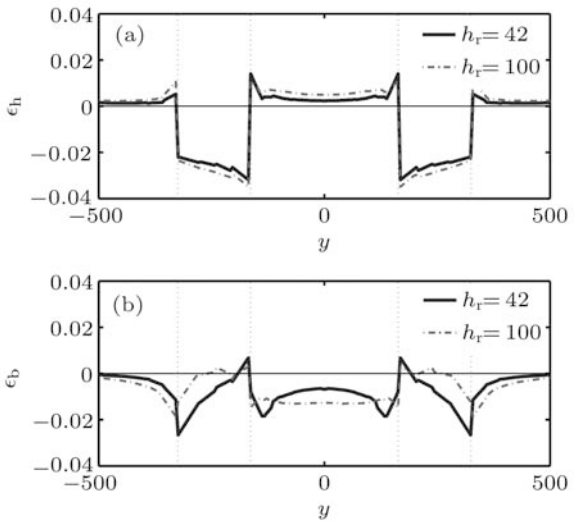


Fig. 3. Plots of (a) $\epsilon_{\rm h}$ and (b) $\epsilon_{\rm b}$ strains at $z = 0$ versus QR height along the y axis.

As shown in Fig. 3(a), the hydrostatic strain increases as the height of the QR increases from 42 Å to 100 Å. On the other hand, the bi-axial strain inside the QR shown in Fig. 3(b), which is closely related to the heavy hole subband energy, becomes compressive in the whole region as the height increases.

Figure 4 shows the interband transition energy defined as the difference between the conduction and the heavy-hole subband energy versus inner diameter R_1 and QR height h_r at QR temperature (T) of 30 K. In this calculation, we take the temperature-dependent CdTe bandgap energy as $E_g(T) = E_g(0) - \alpha T^2/(\theta_D + T)$, where the zero temperature bandgap energy $E_g(0)$ is 1.923 eV, the Debye temperature Θ_D is 160 K, and the Varshni's proportionality constant α is 4.73×10^{-4} eV·K^{-1}.[33] It is clearly shown that the interband transition energy increases with the increasing inner diameter (or the decreasing QR volume), which is a general trend for the QD heterostructure no matter whether it is strained or not.[15,16] We also note that the interband transition energy deceases slightly as the height increases from 42 Å to 70 Å, which is attributed to the decreasing bandgap energy between the conduction and the valence band edges due to the combined effects of the QR height and the hydrostatic and the bi-axial strains, as shown in Fig. 3.

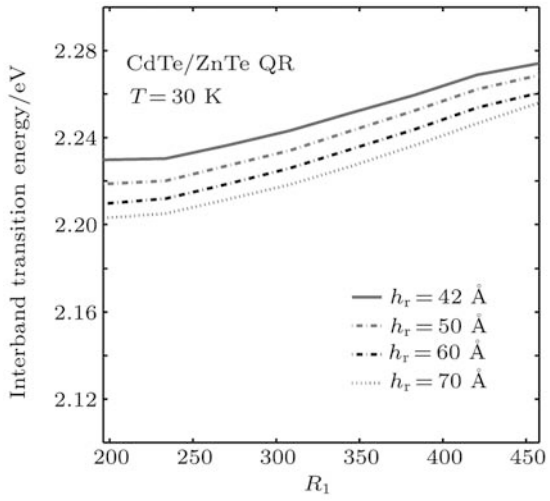


Fig. 4. Interband transition energy versus inner QR diameter R_1 and height h_r at T = 30 K . The interband transition energy increases with increasing R_1 (or decreasing QR volume), while it shifts downward with increasing QR height (or increasing QR volume).

Finally, Fig. 5 shows the interband transition energy as a function of height and temperature of the QR with the same structural parameters as those shown in Fig. 1 except wetting layer width t_w = 2.5 ML, where the squares represent the experimental data taken from the photon minescence spectra.[14] We find that the interband transition energy decrease with increasing QD temperature regardless of the height of the QR, which is mainly due to the temperature-dependent CdTe bandgap energy adopted for this calculation. Our current FEM model is in good accordance with the PL data for the QR height in the range of $32 \le h_r \le 48$ Å, in particular, at h_r = 42 Å.[14]

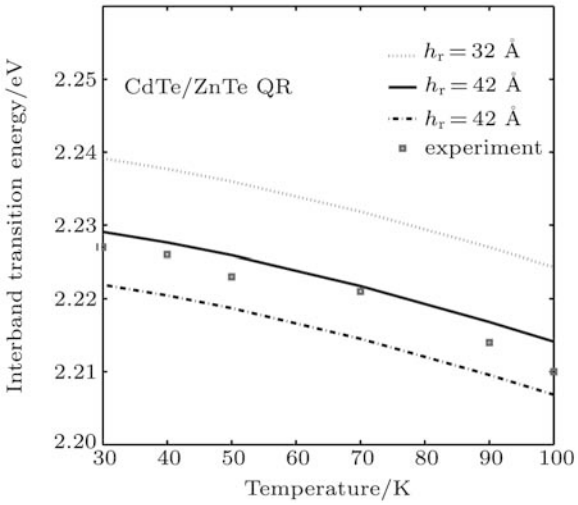


Fig. 5. Interband transition energy versus temperature and height of QR, which is in good agreement with the PL data for the QR height at h_r = 42 Å.[14]

One may speculate whether thermal expansions of the strained QR system can lead to a further deformation in the strain distribution and possible changes in the interband transition energy. In fact, it has been recently demonstrated by Patil and Melnik[34] that the piezoelectricity coupled with the thermal expansion in the CdTe/ZnTe quantum wire shows a weak influence on the strain distributions. However, the conduction band edge of the wire system varies only at very high temperature. The measured temperature range for the experiment in the present work is way below that for the thermal-piezoelectricity effect to affect the energy band structure.[34] In fact, the thermally stable CdTe/ZnTe QR system may be important, since it can preserve the optoelectronic properties of nanostructures under the high temperature operation.

4. Conclusion

The combined effects of the size and temperature on the strain distributions and the electronic structure of CdTe/ZnTe self-assembled QRs are investigated with the finite element method based on the linear elasticity theory of solids and the eight-band

$\boldsymbol{k} \cdot \boldsymbol{p}$ Hamiltonian. We find that the QR height significantly changes the bi-axial strain while it has less effect on the hydrostatic strain, which is related to the conduction and the valance energy bands, respectively, as shown in Fig. 3. According to a thermal dependence model for the CdTe bandgap energy,[33] we show that the calculated interband transition energy is in good agreement with the experimental PL data[14] in the measured temperature range.

References

[1] Grbic B, Leturcq R, Ihn T, Ensslin K, Reuter D and Wieck A D 2008 *Physica* E **40** 1273

[2] Warburton R J, Schulhauser C, Haft D, Schaflein C, Karrai K, Garcia J H, Schoenfeld W and Petroff P M 2002 *Phys. Rev.* B **65** 113303

[3] Troiani F, Hohenester U and Molinari E 2000 *Phys. Rev.* B **62** R2263

[4] Kerr W E, Pancholi A and Stoleru V G 2006 *Physica* E **35** 139

[5] Mackowski S 2002 *Thin Solid Films* **412** 96

[6] Borkovska L V, Korsunska N O, Sadofyev Y G, Beyer R, Weber J, Kryshtab T, Andraca-Adame J A, Kazakov P and Kushnirenko V I 2007 *Phys. Stat. Sol.* (b) **244** 1700

[7] Nguyen T A, Mackowski S, Hoang T B, Jackson H E, Smith L M and Karczewski G 2007 *Phys. Rev.* B **76** 245320

[8] Brault J, Gendry M, Grenet G, Hollinger G, Olivares J, Salem B, Benyattou T and Bremond G 2002 *J. Appl. Phys.* **92** 506

[9] Lee H S, Lee K H, Choi J C, Park H L, Kim T W and Choo D C 2002 *Appl. Phys. Lett.* **81** 3750

[10] Karczewski G, Maćkowski S, Kutrowski M, Wojtowicz T and Kossut J 1999 *Appl. Phys. Lett.* **74** 3011

[11] Lee H S, Park H L and Kim T W 2004 *Appl. Phys. Lett.* **85** 5598

[12] Lee H S, Park H L and Kim T W 2007 *Appl. Phys. Lett.* **90** 181909

[13] Lee H S, Park H L and Kim T W 2008 *Appl. Phys. Lett.* **92** 052108

[14] Kim T W, Lee E H, Lee K H, Kim J S and Park H L 2004 *Appl. Phys. Lett.* **84** 595

[15] Hong W P and Park S H 2009 *J. Korean Phys. Soc.* **55** 1607

[16] Hong W P and Park S H 2009 *J. Korean Phys. Soc.* **55** 2496

[17] Park S H and Hong W P 2009 *J. Korean Phys. Soc.* **55** 2517

[18] Park S H and Hong W P 2010 *Jpn. J. Appl. Phys.* **49** 012801

[19] Park S H and Hong W P 2010 *Chin. Phys. Lett.* **27** 098502

[20] Hong W P and Park S H 2009 *J. Korean Phys. Soc.* **57** 178

[21] Bahder T B 1990 *Phys. Rev.* B **41** 11992

[22] Van de Walle C G 1989 *Phys. Rev.* B **39** 1871

[23] Woo J T, Song S H, Lee I, Kim T W, Yoo K H, Lee H S and Park H L 2007 *J. Appl. Phys.* **102** 033521

[24] Li T, Lozykowski H J and Reno J L 1992 *Phys. Rev.* B **46** 6961

[25] de Paiva R, Nogueira R A, de Oliveira C, Leite Alves H W, Alves J L A, Scolfaro L M R and Leite J R 2002 *Brazilian J. of Phys.* **32** 405

[26] Yamada M, Yamamoto K and Abe K 1977 *Appl. Phys.* **10** 1309

[27] Greenough R D and Palmer S B 1973 *Appl. Phys.* **6** 587

[28] Huebner K H, Dewhirst D L, Smith D E and Byrom T G 2001 *The Finite Element Method for Engineers* (New York: Wiley) p. 250

[29] Noda S, Abe T and Tamura M 1998 *Phys. Rev.* B **58** 7181

[30] Johnson H T, Freund L B, Akyüz C D and Zaslavsky A 1998 *J. Appl. Phys.* **92** 5819

[31] Jin J 2002 *The Finite Element Method in Electromagnetics* (London: Wiley-IEEE Press) p. 223

[32] Kuo M K, Lin T R, Hong K B, Liao B T, Lee H T and Yu C H 2006 *Semicond. Sci. Technol.* **21** 626

[33] Allahverdi Ç and Yükselici M H 2008 N *New J. Phys.* **10** 103029

[34] Patil S P and Melnik R V N 2009 *Phys. Status Solidi* A **206** 960